Numerical Simulation of Keeper Erosion in a 6-kW Laboratory Hall Thruster

IEPC-2015-16／ISTS-2015-b-16

Presented at Joint Conference of 30th International Symposium on Space Technology and Science
34th International Electric Propulsion Conference and 6th Nano-satellite Symposium,
Hyogo-Kobe, Japan
July 4 – 10, 2015

Maria Choi[1] and Iain D. Boyd[2]
University of Michigan, Ann Arbor, MI, 48109, United States

Abstract: A sputtering model is implemented into a hybrid particle-fluid code to describe erosion behavior on a cathode keeper in a Hall thruster. Coefficients of semi-empirical fits to sputtering yields of graphite from xenon ion bombardment at normal and various incidence angles are determined. Incident species energy distributions and fluxes, and mean erosion rates as a function of location on the keeper are calculated from the particle-in-cell method. Plasma properties simulated by the model are compared to experimental data and show good agreements. Changing the plasma potential at the cathode boundary improves the agreement for plasma potential in the cathode plume, and alters the erosion profile, implying that the cathode condition plays an important role in the near-field plume structure.

Nomenclature

A, B	=	normal incidence sputtering yield fitting coefficients
c_0, c_1, c_2	=	angular dependent sputtering yield fitting coefficients
C_i	=	ionization rate coefficient, $m^3 s^{-1}$
D_{th}	=	mean thruster channel diameter, m
e	=	electron charge, 1.6×10^{-19} C
E_{th}	=	threshold energy for sputtering, eV
$\vec{E}$	=	electric field, Vm^{-1}
$\vec{j}$	=	current density, $A\,m^{-2}$
k_B	=	Boltzmann constant, $1.38 \times 10^{-23}\,J\,K^{-1}$
m_e	=	electron mass
M	=	heavy species mass
n_e	=	electron number density, m^{-3}
n_n	=	neutral number density, m^{-3}
T_e	=	electron temperature, K or eV
U_s	=	surface binding energy of target atom, eV
$\vec{v}$	=	velocity, m/s
Y	=	sputter yield, *atoms/ion* or mm^3/C
γ	=	energy transfer factor
ϵ_i	=	ionization energy, eV
θ	=	incidence angle

[1] Graduate Student, Department of Aerospace Engineering, mclang@umich.edu.
[2] James E. Knott Professor of Engineering, Department of Aerospace Engineering, iainboyd@umich.edu.

κ = thermal conductivity, $W\ (K\ m)^{-1}$
ν = collision frequency, s^{-1}
σ = plasma conductivity, $S\ m^{-1}$
σ_{CEX} = charge-exchange collision cross section, m^2
ϕ = plasma potential, V
ψ = electron velocity stream function, $m^{-2}\ s^{-1}$
ω = velocity temperature exponent

I. Introduction

HOLLOW cathodes are a key component of electric propulsion systems such as Hall-effect thrusters (HETs) and ion thrusters. In HETs, a centrally or externally mounted cathode emits electrons to both ionize the propellant in the discharge chamber and neutralize the ion beam downstream of the thruster. The detailed physics of plasma processes, such as the erosion mechanism due to impacts of high-energy ions on the cathode and anomalous electron transport, are not yet well understood. In order to better understand fundamental physical processes in a HET, it is necessary to develop a reliable numerical model that can capture the collision and plasma physics accurately, validated with experimental data.

One of the main life-limiting factors in conventional HETs has been the erosion process of the discharge channel walls due to ion bombardment. In the state-of-the art magnetically shielded thrusters, this erosion has effectively been eliminated as a failure mechanism by shaping magnetic field lines such that the discharge channel walls are shielded from ion bombardment by achieving ideal equipotentialization of the lines of force near the walls.[1,2] The next potential failure mode in a magnetically shielded Hall thruster is the erosion of the cathode and surface of the magnetic-field pole-pieces.[3,4] Although studies to achieve long cathode life have been conducted in the past,[5,6] it is necessary to investigate the cathode life in a magnetically shielded thruster to identify solutions to eliminate possible wear mechanism as life-limiting factors of the thruster.

This study is concerned with developing an accurate physics-based model to simulate the near-field plume, including the cathode plume, of a Hall thruster. In this paper, a sputtering model is implemented into a 2-D axisymmetric hybrid particle-fluid code called MPIC as a tool to describe the steady state erosion behavior of the cathode keeper in a 6-kW laboratory Hall thruster (H6). The sputtering model can also be used to simulate the erosion profile on the thruster pole-pieces in magnetically shielded thrusters in the future.

Section II of this paper reviews the details of the numerical model and boundary conditions. Section III presents a series of simulation results and a comparison of the results with experimental data. Finally, Section IV summarizes concluding remarks and future work.

II. Numerical Model

The numerical simulation tool utilized in this study is a two-dimensional axi-symmetric hybrid particle-fluid code MONACO-PIC (MPIC)[7] which is capable of simulating non-equilibrium, rarefied flows. The particle-in-cell (PIC) module simulates the transport of all heavy species including the effects of electrostatic fields on the ions by calculating charge density at the nodes in the mesh. The direct simulation Monte-Carlo (DSMC) module handles collisions between heavy species, i.e., neutrals and ions. The electrons are simulated as a fluid by solving conservation laws.

A. Collision Dynamics

To simulate collisions between heavy species, i.e., Xe, Xe^+, and Xe^{2+}, the DSMC method is utilized, where a macroparticle represents a large number of real particles. Momentum exchange (MEX) and charge exchange (CEX) collisions are two basic classes of important collision mechanisms in the plume of a Hall thruster. Collision mechanisms implemented in the current model are the MEX collision between neutral-neutral and neutral-ion pairs, and the CEX collision between neutral-ion pairs. In the DSMC module, a list of colliding particle pairs in each cell are selected at random, regardless of their relative positions and velocities, to perform binary collisions. The collision probability of each pair is calculated at each time step, and is proportional to the product of the relative velocity between the colliding particles and the total cross-section. For the neutral-neutral collisions, the variable hard sphere

(VHS)[8] model is employed. The MEX cross-section for neutral-ion elastic collisions is equivalent to the CEX cross section, as demonstrated by Boyd and Dressler.[9] The CEX cross-section between neutral and ion was measured by Miller *et al*.[10] and parameterized as follows:

$$\sigma_{CEX}(Xe, Xe^{+}) = 10^{-20}(87.3 - 13.6\log_{10}(E))\ m^2 \tag{1}$$

$$\sigma_{CEX}(Xe, Xe^{2+}) = 10^{-20}(45.7 - 8.9\log_{10}(E))\ m^2 \tag{2}$$

where E is collision energy in eV. Once the collision probability is calculated, it is compared with a random number to determine whether a collision occurs or not. If a collision happens, the post-collision velocity and scattering angles are calculated using conservation of linear momentum and the differential cross-section, respectively. Post-collision velocities for a MEX collision are assumed to follow isotropic scattering. For CEX of neutral-ion collisions, a differential cross-section is used due to a strong forward-scattering tendency. The CEX differential cross-section employed in this study was described in Ref. [10] for a Hall thruster plume.

B. Plasma Dynamics

The PIC module tracks the motion of all heavy particles, including the effects of electrostatic fields on the ions. The charge density at each node is calculated from the distribution of the charges. The charge density is used to compute the potential at each node using a fluid electron model. Then, the electric field is calculated by spatially differentiating the electric potential. The electric field is converted into the electrostatic force, which causes acceleration on the charged particles. Quasi-neutrality is assumed to obtain the electron density from the ion number density.

The simplest fluid electron model is the Boltzmann relation, which is one of the most widely used electron models in plasma simulation:

$$\phi = \phi_r + T_e \ln\left(\frac{n_e}{n_r}\right) \tag{3}$$

where ϕ is electric potential, T_e is electron temperature in eV, n_e is electron density, and the subscript r indicates a reference state. The Boltzmann relation is obtained from the electron momentum equation using strong assumptions, such as that the electron fluid flow is isothermal, electron pressure obeys the ideal gas law, and magnetic fields are neglected. These assumptions are not accurate, especially in the near-field plume of a Hall thruster.

In order to increase the level of physics as compared to the Boltzmann relation, a detailed fluid electron model was proposed.[11] The detailed model solves the continuity, momentum, and energy conservation equations that describe the electron fluid at steady state, and is capable of representing more detailed descriptions for electron temperature, velocities, and plasma potential. By introducing a stream-function, ψ, such that $\nabla\psi = n_e\vec{v}_e = \vec{j}_e/e$, and manipulating the equations into convenient forms for numerical solution, the following Poisson-type equations are solved:

$$\nabla^2\psi = n_e n_n C_i \tag{4}$$

$$\begin{aligned}\nabla\cdot(\sigma\nabla\phi) &= \frac{k_B}{e}\left[\sigma\nabla^2 T_e + \sigma T_e \nabla^2\ln(n_e) + \sigma\nabla\ln(n_e)\cdot\nabla T_e\right] \\ &+ \frac{k_B}{e}\left[T_e\nabla\sigma\cdot\nabla\ln(n_e) + \nabla\sigma\cdot\nabla T_e\right]\end{aligned} \tag{5}$$

$$\begin{aligned}\nabla^2 T_e &= -\nabla\ln(\kappa_e)\cdot\nabla T_e + \frac{1}{\kappa_e}\left[-\vec{j}\cdot\vec{E} + \frac{3}{2}n_e(\vec{v}_e\cdot\nabla)k_B T_e\right] \\ &+ \frac{1}{\kappa_e}\left[3\frac{m_e}{M_i}\nu_e n_e k_B(T_e - T_h) + n_e n_n C_i \epsilon_i\right]\end{aligned} \tag{6}$$

From Eqs. (4)-(6), more detailed distributions of three fundamental plasma parameters, $\vec{v}_e$, ϕ, and T_e respectively, are computed using a generalized finite element solver.[7]

C. Sputtering Model

The erosion rate can be calculated as the product of incident flux on the walls and the sputter yield. The incident flux is recorded whenever particles cross the wall boundary from an inner cell, using the PIC algorithm. The sputter yield, Y, is determined by fitting functions for energy dependent yield at normal incidence, $Y(E)$, and for angle-dependent yield, $Y(\theta)$:

$$Y = Y(E)Y(\theta) \tag{7}$$

The energy dependent yield for ions impacting the wall at normal incidence can be calculated from[12,13]:

$$Y(E) = A\sqrt{E}\left(1 - \sqrt{\frac{E_{th}}{E}}\right)^{B} \tag{8}$$

where E is the total energy of the projectile atom impacting the wall, E_{th} is the threshold energy below which sputtering does not occur, and A and B are coefficients fit to experimental data. Traditionally, B for a carbon target is 2.5, but we are using it as a free parameter to best fit experimental data. Although sheath is not resolved in the model, the total energy of an ion is the sum of its direct kinetic energy and the sheath potential energy since ions must transverse a sheath before striking the wall. Assuming there is no secondary electron emission, the sheath potential is:

$$\phi_s = \frac{k_B T_e}{e}\ln\left(\frac{M}{2\pi m_e}\right)^{\frac{1}{2}} \tag{9}$$

where M is the mass of the ion and m_e is the electron mass.

The keeper in the H6 thruster is made of graphite.[3] Most published theoretical work[12,14] predict a threshold energy higher than 130 eV for xenon ions bombarding a carbon target, but more recent experiments[15,16] show that sputtering does occur at or below 50 eV. Although there is no accurate threshold energy data for graphite, Ref. [17] reports that modeling results better match experimental data if the accumulation of xenon in graphite is accounted for. This means that some fraction of the projectiles are carbon as well as that some fraction of the target atoms are xenon. Including this effect, a modified threshold energy can be calculated as 36.5 eV using the equation below[17]:

$$\frac{E_{th}}{U_s} = \frac{1 + 5.7(M_1/M_2)}{\gamma}, \quad M_1 \le M_2 \tag{10}$$

where U_s is the surface binding energy of the target solid in eV, γ is an energy transfer factor in the elastic collision, and M_1 and M_2 are the masses of the projectile and target atom, respectively. The threshold energy of 36.5 eV is used in the current sputtering model in MPIC, since it is in good agreement with the experimental results.[15,16]

The angular dependent yield relative to the normal incidence is[13]:

$$Y(\theta) = 1 + c_0[1 - \cos(c_1\theta)]^{c_2} \tag{11}$$

where θ is the angle relative to the wall normal and c_0, c_1, and c_2 are coefficients to be fit to experimental data.

Experimental measurements of the sputtering yields of various forms of carbon and graphite from xenon ion bombardment at normal incidence[15,16,18-20] are plotted in Fig. 1a. Based on these data, coefficients to the fitting function in Eq. (8) are determined as $A = 0.013$ and $B = 3$. Experimental measurement of sputtering yields at various incidence angle[21] are normalized and shown in Fig. 1b with its fitting function. The coefficients for Eq. (11) are determined as $c_0 = 0.91$, $c_1 = 2.5614$, and $c_2 = 1.91$.

The sputtering model is activated when the simulation starts sampling for macroscopic parameters after steady state has been reached. During the sampling period, the energies and fluxes of the incident particles onto the wall surfaces are recorded to calculate the erosion rate each time step. The erosion rate is summed up during the sampling period and divided by the number of sampling time steps at the end of simulation to determine the mean erosion rate. The resulting mean erosion rate is obtained as a function of position along the keeper surface. Although the implemented model can be applied to calculate sputtering and erosion rates on any walls, only keeper erosion is calculated in this study.

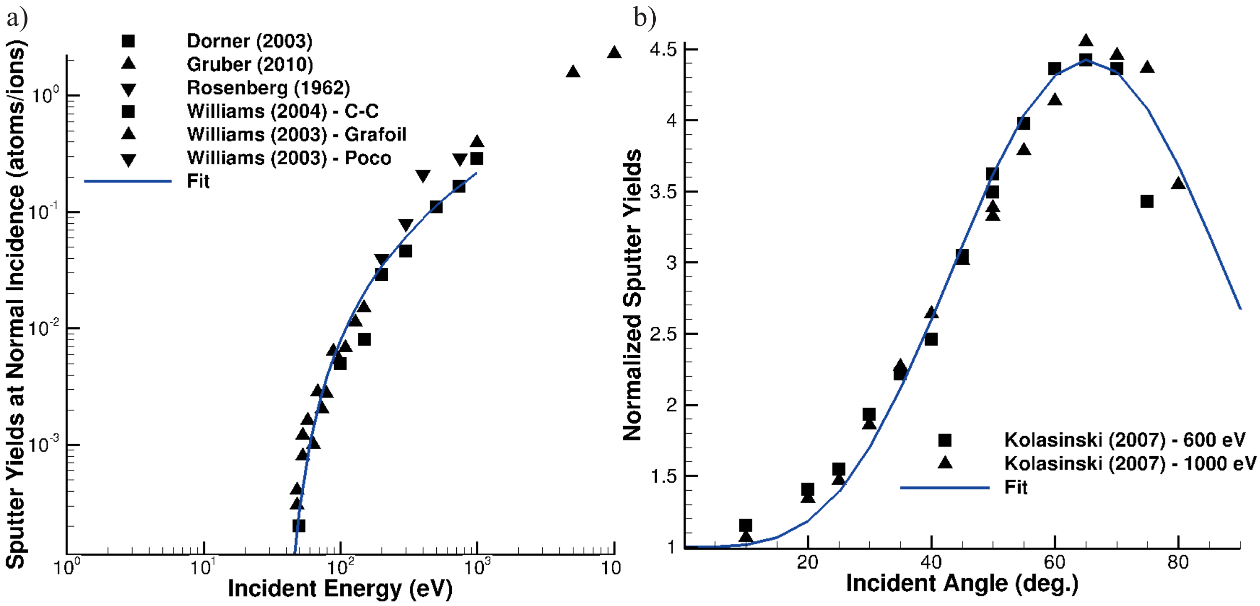

Figure 1. Experimental data and fitting functions of: a) sputter yield at normal angle incidence[15,16,18-20] using coefficients $A = 0.013, B = 3$, and $E_{th} = 36.5$ eV to Eq. (8), and b) normalized sputter yield at various incident angles with incident ion energy of 600 eV and 1000 eV[21] using coefficients $c_0 = 0.91, c_1 = 2.5614$, and $c_2 = 1.91$ to Eq. (11).

D. Computation Domain and Boundary Conditions

The plume of the 6-kW laboratory Hall thruster, including the center-mounted cathode plume, is simulated. A computational grid and a schematic of the boundary conditions of the simulation domain are shown in Fig. 2a and b, respectively. The computation domain extends to $Z/D_{th} = 3.1$ along the axis of symmetry from the thruster exit plane and to $R/D_{th} = 1.5$ radially from the centerline of the cathode. The keeper wall in the current study corresponds to only the wall at the exit plane of the thruster, as shown in Fig. 2b. The curved channel inflow surface, initially proposed by Huismann,[22] is chosen to avoid magnetic field effect which is the strongest inside and in the near-field plume of the discharge channel and diminishes rapidly as distance away from the thruster exit plane increases. Utilizing this inflow shape showed improved results in previous simulation.[23]

Boundary conditions must be specified at each inflow boundary (i.e., cathode exit and discharge channel exit), along the outer edges of, and along all walls in the computational domain. Specifically, the plasma potential, electron temperature, and electron current density for the electron model, and the number density, velocity, and temperature for each of the heavy species are required. Since no experimental data are available to provide all these requirements, available internal plasma simulation results of a hollow cathode and the discharge chamber were utilized to provide inflow boundary conditions, as described in Ref. [23]. The conditions at the cathode exit plane were extracted from results provided by Jet Propulsion Laboratory's hollow cathode code OrCa2D[24] and the conditions at the discharge channel inflow boundary were provided by HPHall simulation[22].

Since Poisson-type equations are solved for the electron model, Eqs. (4-6), either Dirichlet or Neumann conditions are required at each boundary. The mean values of plasma potential with respect to the facility ground and electron temperature at the cathode inflow boundary are 5.5 V and 3.1 eV, respectively. The gradients of electron temperature and plasma potential normal to the boundary at the symmetry line are set to zero. The electron temperature and potential at outflow boundaries are set to constant values. At the wall boundaries, the gradients of plasma potential and electron temperature normal to the surfaces are set to zero. The temperatures of the keeper and pole-pieces are assumed as 773 K and 300 K, respectively. Any ions colliding with the walls are neutralized, and diffuse reflection is assumed.

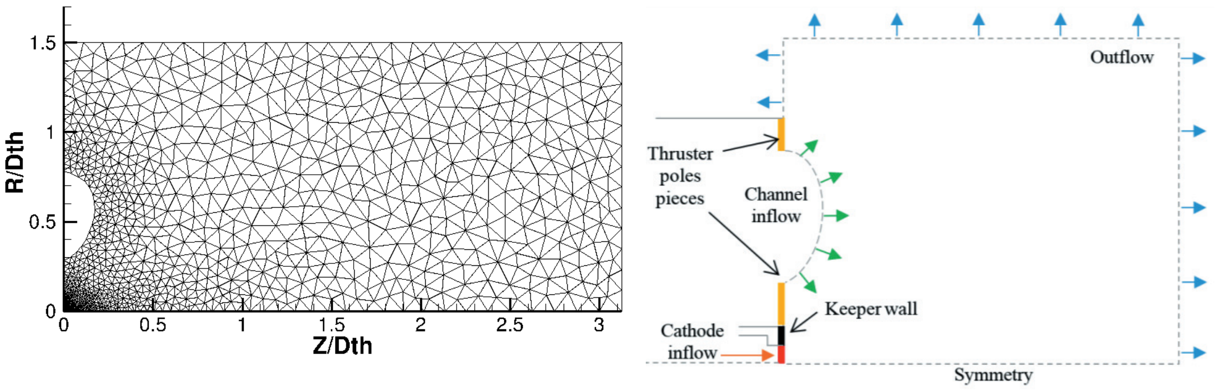

Figure 2. Computational grid for 2-D axi-symmetric modeling of a 6-kW laboratory Hall thruster plume (left). A schematic of boundaries including the symmetry line, outflow, walls, and inflow boundaries (right).

III. Simulation Results

The hybrid particle-fluid plume model, MPIC, described in Section II is utilized to simulate the plume of the H6 Hall thruster. The domain consists of 2,016 triangular cells, and approximately 5.1 million particles are employed. The time step size is 4.2×10^{-8} seconds. The plume simulation runs for 180,000 time steps to reach a steady state, and then for another 100,000 steps to sample plasma and flow data. The simulation is run in parallel on the FLUX cluster at the University of Michigan Center for Advanced Computing. The cases reported here are run utilizing 24 cores with a computational wall time of approximately 29.3 hours.

In this section, a series of simulation results are presented, accompanied by comparisons made with measurements taken by Jameson[25] and Reid[26] for the H6 thruster operated at the following nominal conditions: discharge voltage of 300 V, discharge current of 20 A, anode flow rate of 20 mg/s of xenon, and cathode flow rate measuring 7% of the anode flow. Then, the results of sputtering model is presented, followed by the sensitivity study of cathode boundary condition on simulation results.

A. Plasma Properties and Comparison with Experimental Data

Comparisons are made between the numerical simulation results and available experimental data.[25,26] For the data measured by Jameson,[25] the background pressure during the thruster operation was 1.7×10^{-5} Torr. The plasma potential was measured with an emissive probe, with uncertainty of ± 1 V. Ion current density measurements were performed by Reid[26] using two Faraday cup probes. The experimental data by Reid had approximately the same background chamber pressure during the thruster operation as Jameson. The uncertainty associated with Reid's near-field probe measurements is $\pm 10\%$, whereas the far-field probe measurements have $\pm 0 - 50\%$ on the integrated beam current. Simulation using MPIC is performed at the same background gas pressures as the experiments.

In Fig. 3, contours of a) plasma potential, and b) electron temperature are shown. Both the potential and electron temperature gradually decrease away from the thruster channel. A quantitative comparison of plasma potential is made with the measurements in Figs. 4 and 5. As shown in Fig. 4, the model reproduces reasonably well the measured plasma potential profile along the cathode centerline, predicting a slightly higher value than the measurements by 6 V at the cathode inlet ($Z/D_{th} = 0$) and by 4 V at $Z/D_{th} = 1.38$.

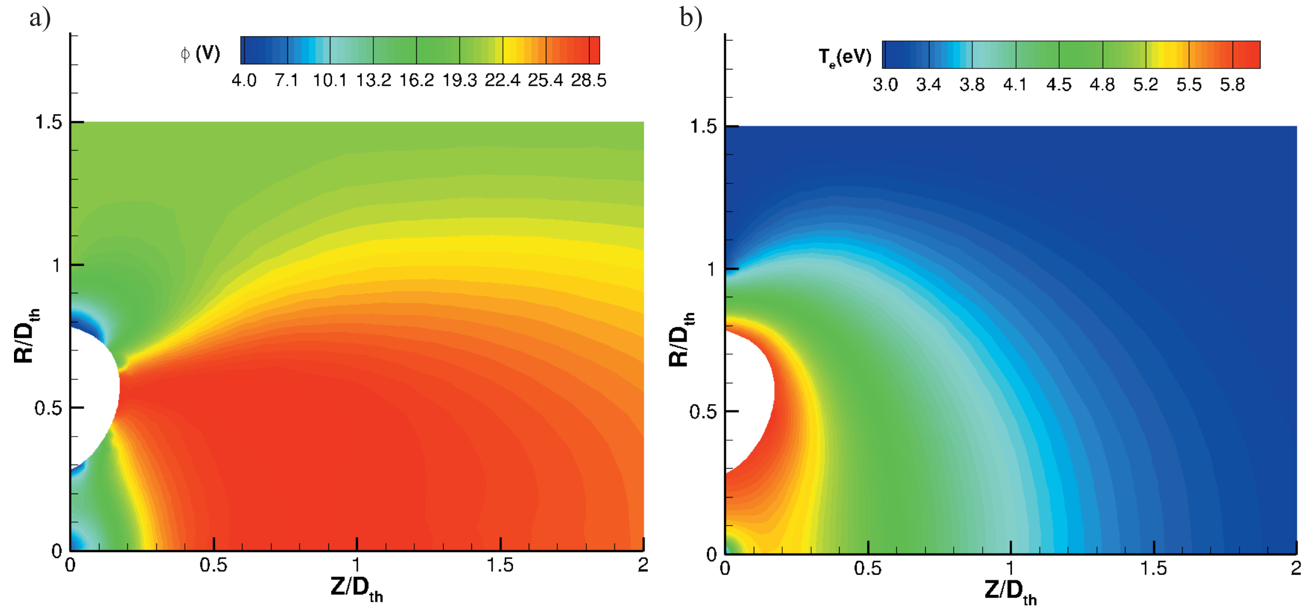

Figure 3. Contour plots of a) plasma potential, and b) electron temperature, from MPIC simulation.

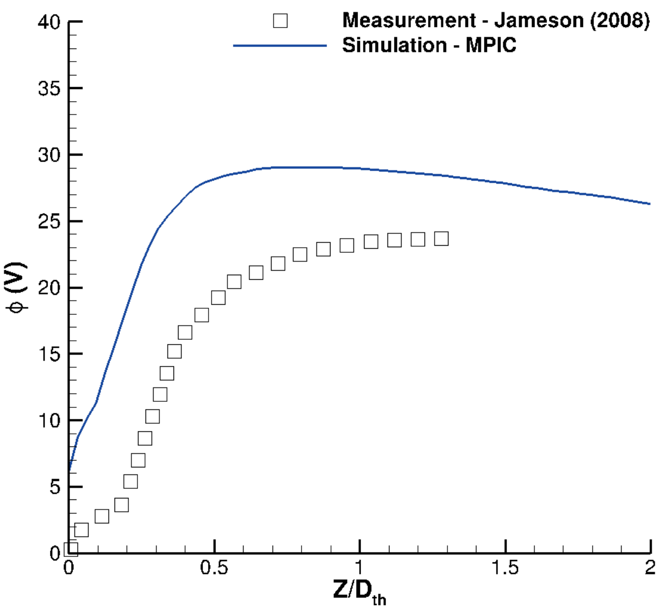

Figure 4. Comparison of axial profiles of plasma potential with respect to a facility ground.

The radial profiles of plasma potential in the near-field and far-field plume are shown in Fig. 5a and b, respectively. Here, the simulation profiles show reasonably good agreement with and similar shape as the measurements away from the cathode centerline. A shift radially outward of the peak potential around the channel centerline ($R/D_{th} = 0.5$) is observed in Fig. 5a. This shift may be due to the boundary condition imposed at the discharge channel inflow which was extracted from an HPHall simulation result.

Contour plots of ion current density from the experimental measurement[26] and numerical simulation are compared on the top and bottom, respectively, in Fig. 6. While the magnitude and shape of the contours look similar, the high current density measured in the cathode plume is not predicted by the model. The model shows a slight rise in current density along the centerline at about $Z/D_{th} = 2$, although its magnitude is lower than the measured value.

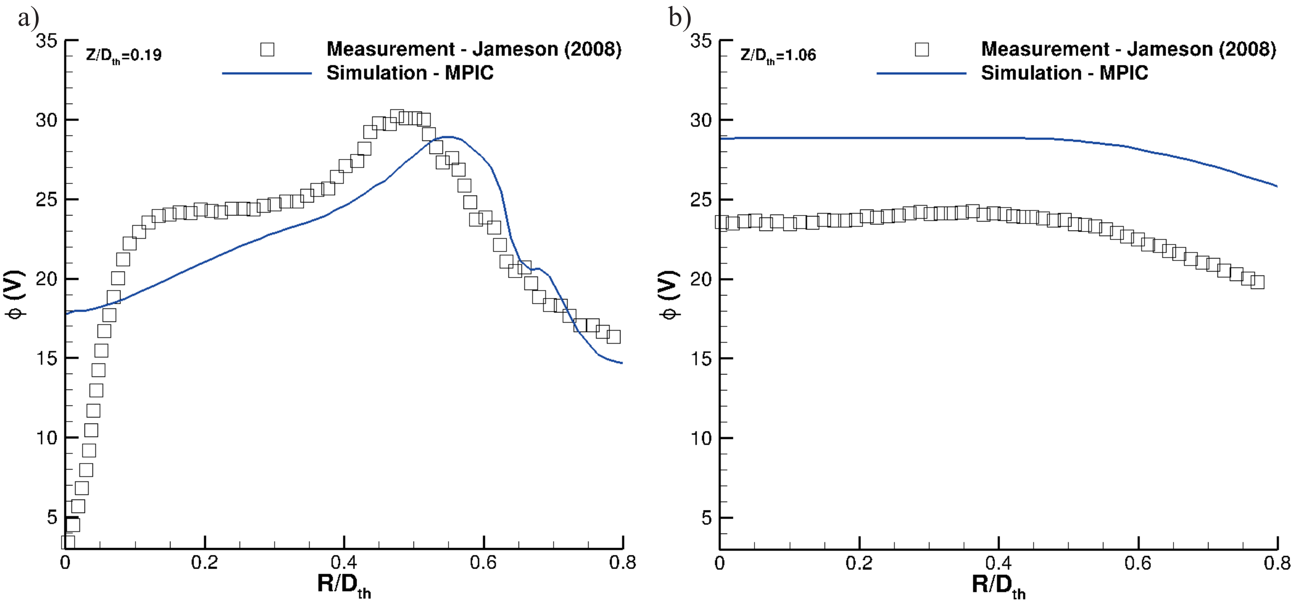

Figure 5. Comparison of radial profiles of plasma potential a) at Z/D$_{th}$ = 0.19, and b) Z/D$_{th}$ = 1.06.

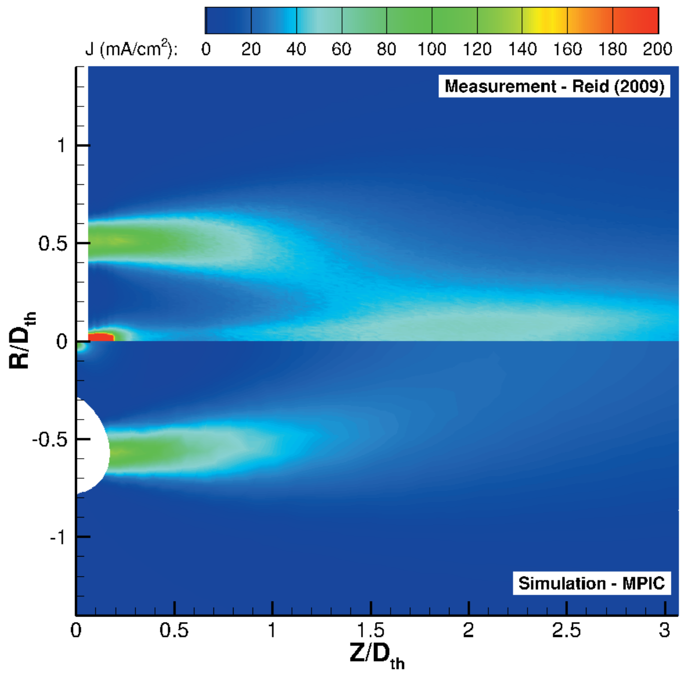

Figure 6. Contour plots of ion current density: experimental data[25] (top), and numerical simulation (bottom).

A more quantitative comparison is made by plotting ion current density along the plume axis in Fig. 7. The minimum value occurs at Z/D$_{th}$ = 0.5 in both the experimental data and simulation result. There is a large difference between the measurement and numerical simulation near the cathode centerline as previously seen in contour comparison in Fig. 6. However, the simulation predicts ion current density quite well further downstream. A similar observation is made from the radial ion current density profiles in Fig. 8 in both a) near-field, and b) far-field plume. There is approximately a 210 mA/cm^2 difference between the measurement and simulation results at the cathode centerline in the near-field, and a 30 mA/cm^2 difference in the far-field. The simulation predicts the same magnitudes as the experimental measurement at radii greater than 0.2 away from the cathode centerline. In the near-field plume, there is a shift in the peak current density at the channel exit at $R/D_{th} = 0.5$, which was also observed in the plasma potential in Fig. 5a.

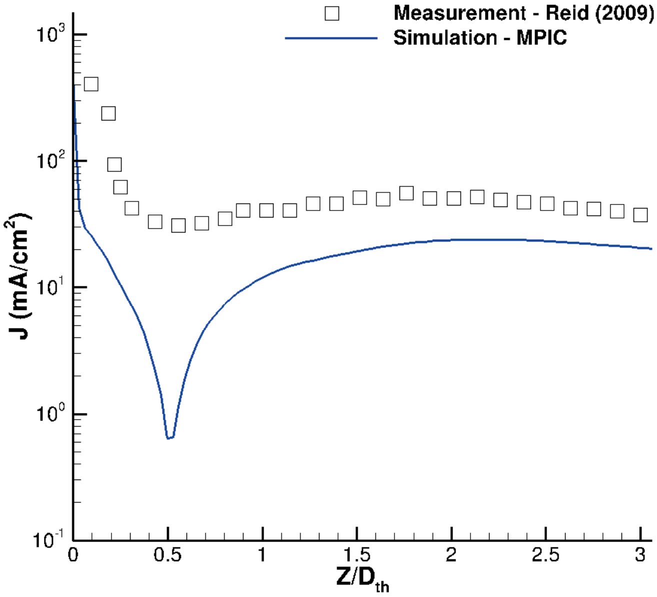

Figure 7. Comparison of axial profiles of ion current density.

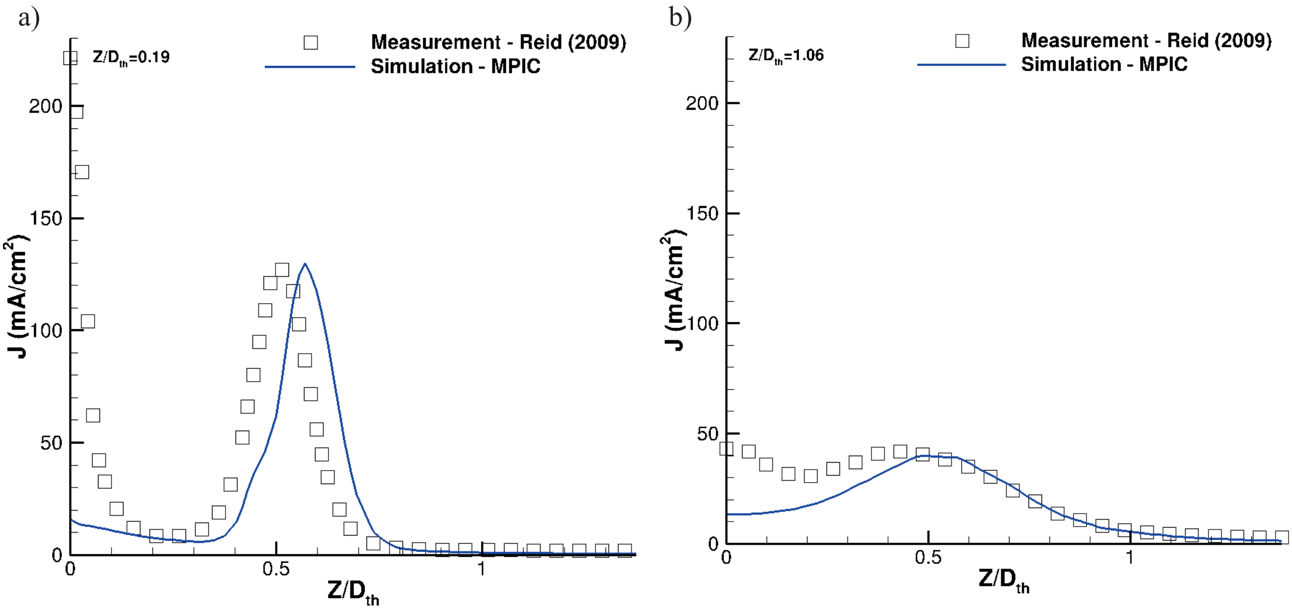

Figure 8. Comparison of radial ion current density profiles: a) at $Z/D_{th} = 0.19$, and b) $Z/D_{th} = 1.06$.

B. Sputtering Results

The sputtering model described in the previous section is utilized to simulate the erosion behavior on the exit plane of the keeper wall. The keeper wall consists of six computational cells, and the results are shown with normalized radial displacements from 0 to 1. When a particle hits the keeper surface, its energy and incident flux are recorded on each surface element to calculate the sputter yield and erosion rate.

In Fig. 9, the incident energy distributions of xenon neutrals, single-charged and double-charged ions are plotted. Cell 1 corresponds to the radially inner-most cell and cell 6 corresponds to the cell located furthest away from the cathode centerline. The energy distributions in y-axes are in arbitrary unit. Figure 9a shows that the majority of the neutrals have low energy, and very few of them have high-enough energy to contribute to the sputtering of the wall. The neutrals hit the keeper uniformly on each cell. Figure 10a shows that the neutral flux on keeper is almost about one to two orders of magnitudes higher than Xe^{+} and Xe^{2+} ions.

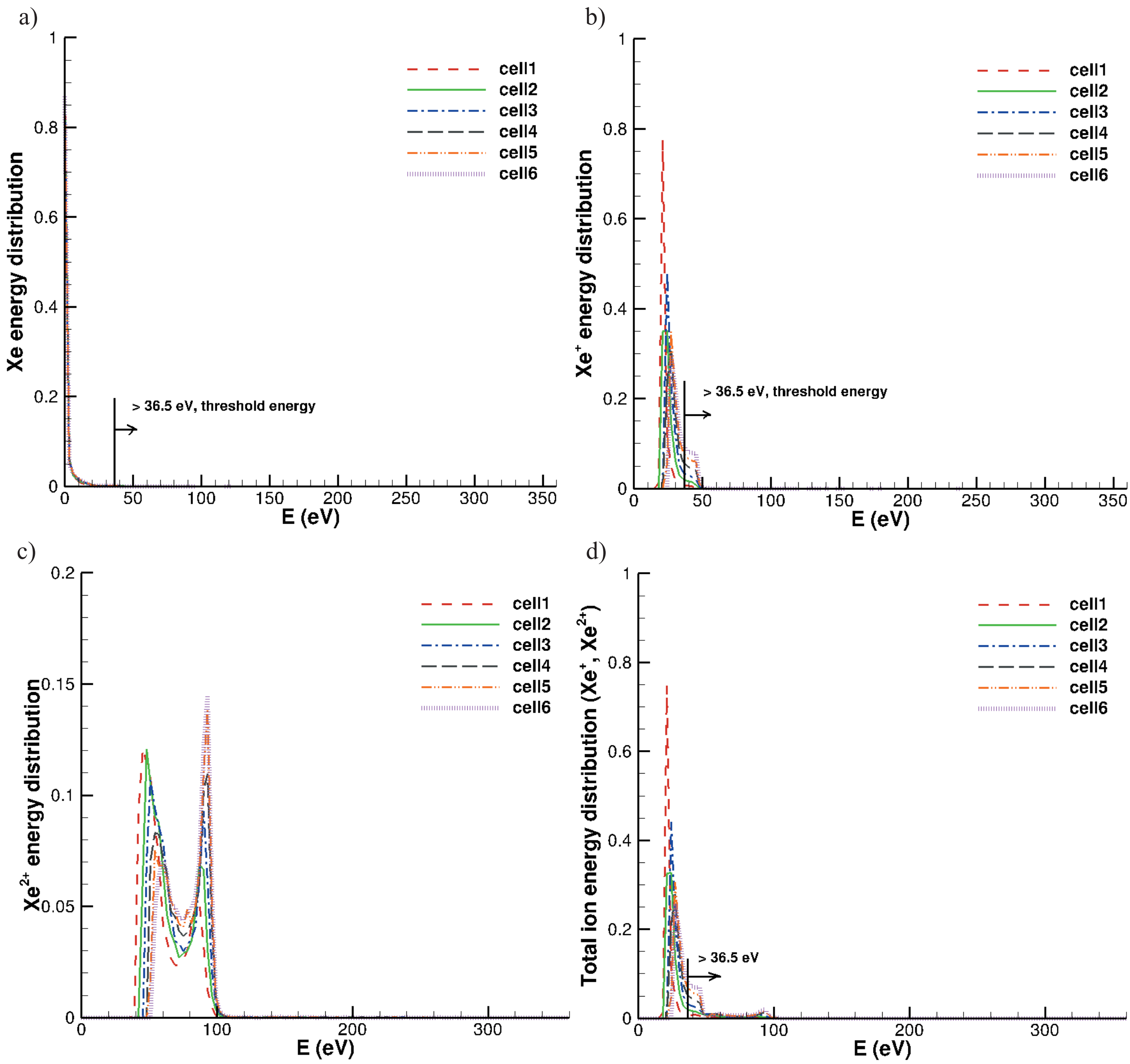

Figure 9. Incident species energy distributions on the keeper wall: a) Xe neutrals, b) Xe^{+} ions, c) Xe^{2+} ions, and d) all ion species.

The energy distributions of Xe^+ ions on the keeper walls are shown in Fig. 9b. Not all of the Xe^+ ions have energy greater than the threshold energy of 36.5 eV. According to the small shifts observed in the first two highest peaks in the lower energy range (<50 eV), the ions hitting the cells located at lower radii have lower energies than the ions hitting the cells at larger radii. These low-energy ions gain energy through the sheath potential that is proportional to electron temperature, as in Eq. (9). According to the electron temperature profile on the wall shown in Fig. 10b, ions accelerate through a slightly greater sheath potential for cells at larger radii than the cells at smaller radii because T_e is slightly greater at larger radii. In Fig. 10a, the flux of Xe^+ ions hitting cell 1 is the highest due to having the lowest plasma potential and its location. A similar trend is observed for double-charged ions, as the energy peak for the lower energy range is shifted slightly to the right for cells at larger radii, as shown in Fig. 9c. Almost all of the Xe^{2+} ions hitting the keeper can contribute to sputtering of the surface.

The total ion energy distributions (i.e., Xe^+ and Xe^{2+}) are shown in Fig. 9d, where multiple peaks occur as a result of multiple charge-exchange collisions. This study shows that the ions in the lower energy range are mainly due to the energy gained through the sheath potential drop, as a function of electron temperature, while the ions at higher energy range are more affected by the wall potential.

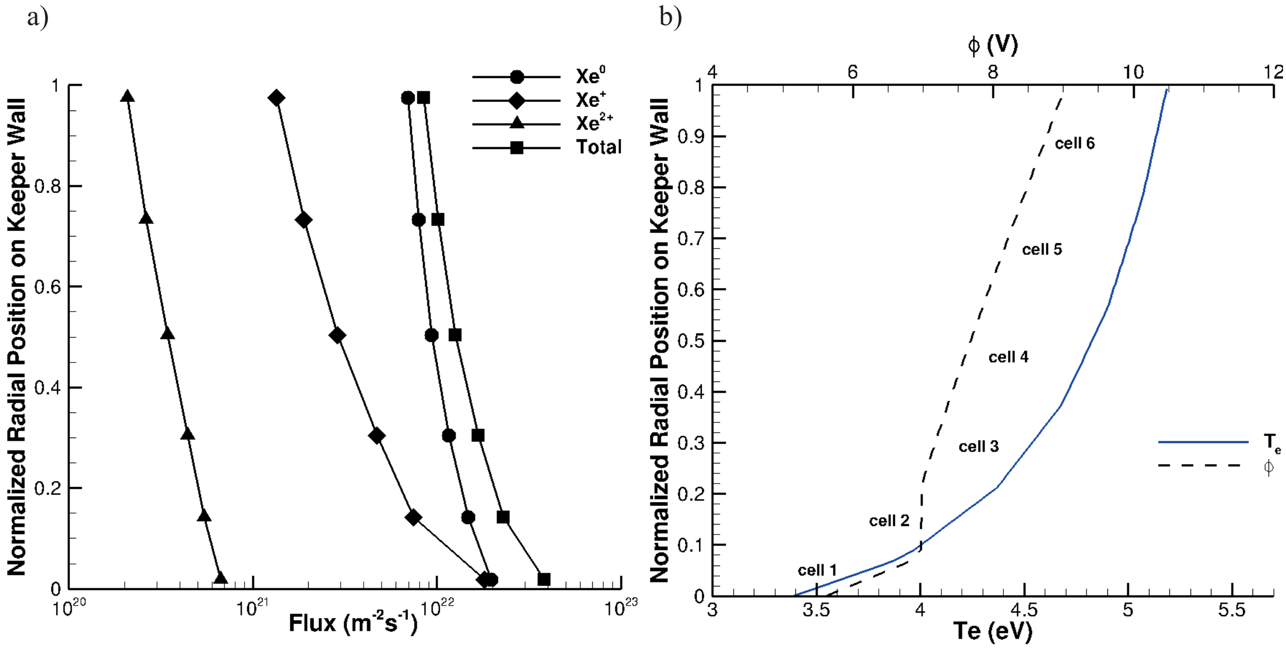

Figure 10. a) Incident species flux, and b) plasma potential and electron temperature on the keeper wall as a function of normalized radial positions

Figure 11 shows the mean erosion rates as a function of radial location of the keeper for all species. The erosion of the keeper mainly arises from Xe^{2+} ions. Although their flux is much lower than Xe neutrals and Xe^+ ions, shown in Fig. 9a, their incident energy is much greater than the threshold energy unlike most of the neutrals and single-charged ions. Since the potential profile along the keeper (Fig. 10b) decreases from the cells at larger radii to the cells at smaller radii, the cells at smaller radii, especially cell 1, attract a larger flux of each charged species. However, particles go through more collisions—both MEX and CEX—near the cathode due to the higher neutral flux in that region, so the incident species energies at cell 1 are not necessarily the largest.

Although there are no keeper erosion measurements for the H6 thruster available, the calculated mean erosion rate is compared with the published erosion rate of the discharge channel wall, also known as the insulator ring, from Ref. [2], shown in Table 1. The estimated mean erosion rate of the keeper wall is approximately 0.1 $\mu m/h$ which is approximately five time higher than the measured erosion rate of the inner channel wall of the magnetically shielded (H6MS) thruster, and about two orders of magnitude lower than the erosion rates of both the inner and outer rings of the unshielded (H6US) thruster.

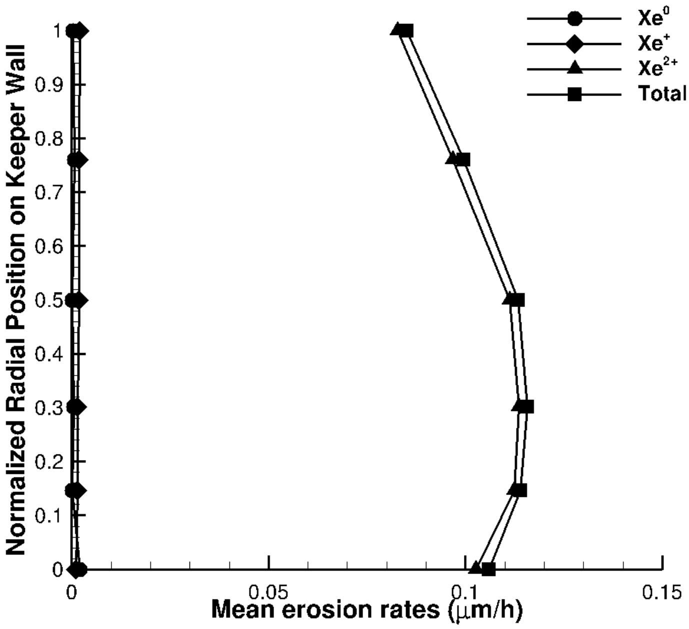

Figure 11. Mean erosion rates caused by each and all species.

Table 1. Summary of measured erosion rates of the discharge channel walls of the H6US and H6MS thrusters.[2]

	Axial Position (Z/L_{ch})	Erosion Rate (μm/h)
Unshielded - outer ring	0.973	15.0
Unshielded - inner ring	0.973	19.7
Magnetically shielded - outer ring	0.947	0.0
Magnetically shielded - inner ring	0.947	0.02

C. Effect of Cathode Exit Condition

Overall, the simulation can predict the experimental measurement quite well, except in the cathode plume which may be a key region in keeper erosion modeling. Since the measured plasma potential at the cathode is closer to 0 V[24] rather than 5.5 V, the cathode potential boundary condition is changed from 5.5 V to 0 V to test how sensitive the plume structure is to this condition. In Fig. 12a, the simulation profile for plasma potential obtained with $\phi_{cathode} =$ 0 V shows improved agreement with the experimental measurement near the cathode. The simulated plasma potential merges to the same value further downstream in both cases. A similar observation is made for the ion current density comparison in Fig. 12b that current density is slightly increase in the near-field plume but does not affect the far-field plume.

The effect of cathode potential on the plasma potential and mean erosion rates along the keeper wall is shown in Fig. 13. While electron temperature (not shown) is unchanged, a lower potential on the wall using $\phi_{cathode} = 0$ V attracts a higher ion flux to bombard the surface, resulting in approximately 1.7 times greater mean erosion rates than the rate predicted by using a cathode exit potential of 5.5 V.

Applying a 0 V potential at the cathode inlet does not change the results in the far-field but improves the plasma potential profile in the near-field plume, implying that the cathode condition plays an important role in the near-field plume structure and erosion behavior on the keeper. The OrCa2D simulation result used as the inflow boundary condition at the cathode did not include the magnetic field effects which may contribute to the poor agreement in the cathode plume. In addition, the predicted erosion profile may change with implementation of the magnetic fields in the electron fluid module in MPIC.

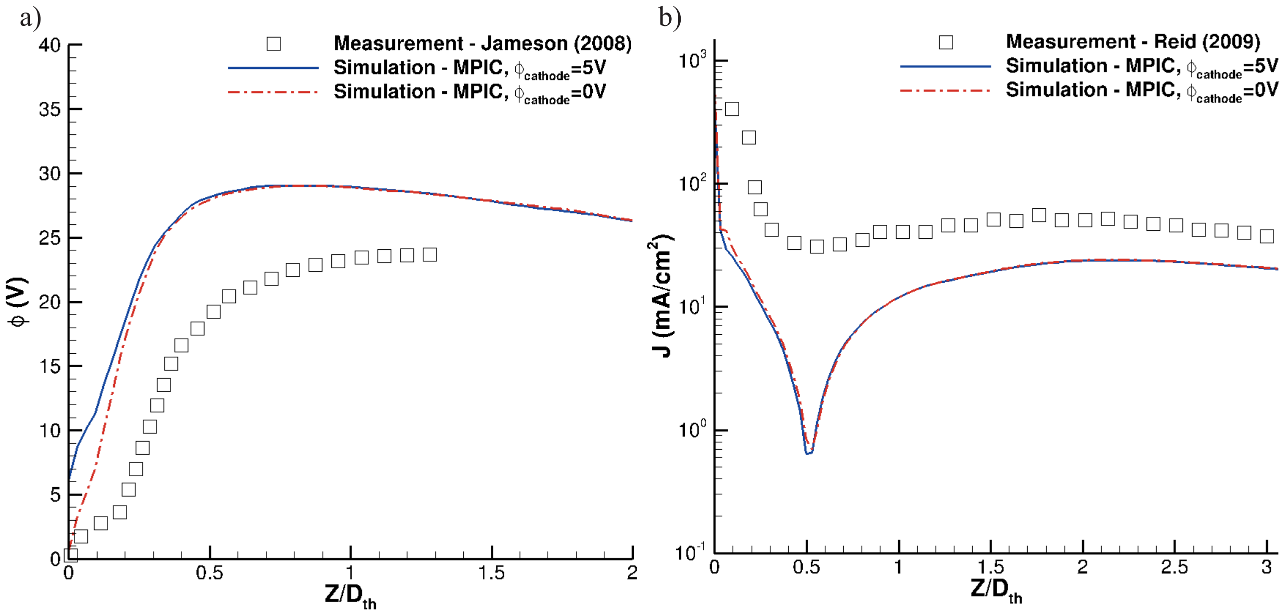

Figure 12. Comparison of simulation results along the plume axis obtained with two different potentials at the cathode boundary: a) plasma potential, and b) ion current density.

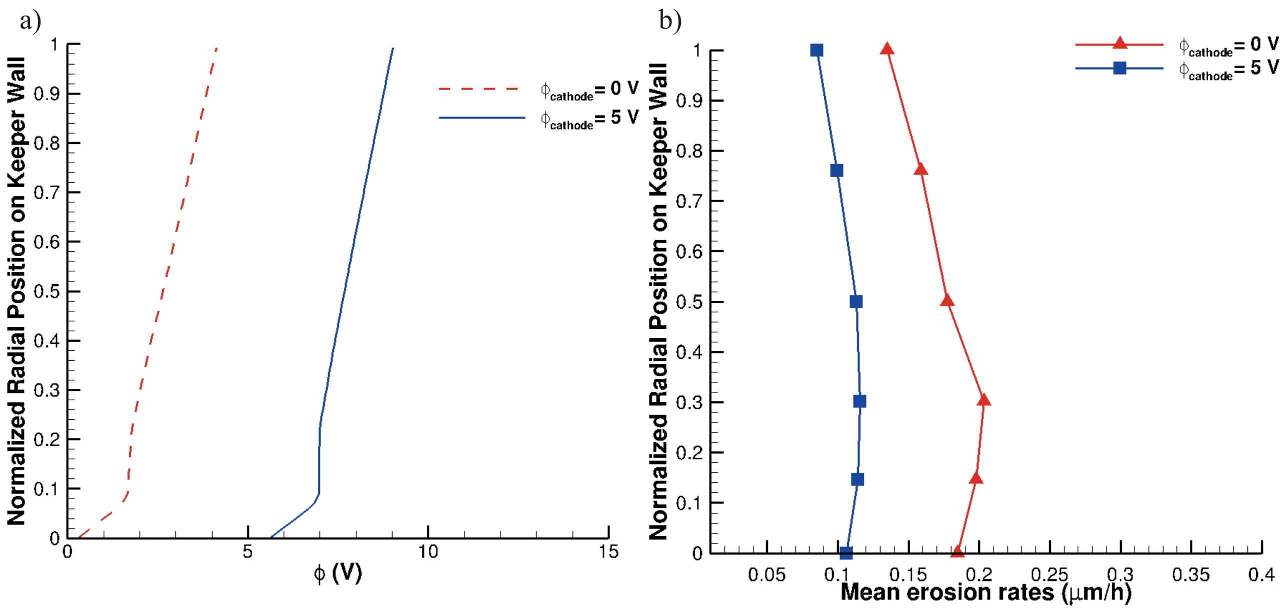

Figure 13. Effect of the assumed cathode potential on keeper wall properties as a function of normalized radial position: a) plasma potential, and b) mean erosion rate.

IV. Conclusion

As an effort to develop an accurate, physics-based numerical tool to simulate fundamental physical processes in a Hall thruster plume and its cathode, a sputtering model was implemented in MPIC which is a 2-D axis-symmetric hybrid particle-fluid plume code. This study determined the profiles of mean erosion rate on the wall at the exit plane of the cathode keeper in order to quantify the potential failure mechanism due to erosion. The calculated mean erosion rate of the keeper is comparable with that for erosion of the discharge channel in a 6-kW magnetically shielded Hall thruster,[2] although it may depend on the operating conditions on the thruster. The sputtering model implemented into MPIC can be utilized to describe the erosion behavior of other walls, such as the thruster pole pieces in magnetically shielded thrusters in the future. Such work requires improving the electron fluid module to account for the magnetic field to account for the differences in the designs of the magnetically shielded and unshielded thrusters. In addition, the predicted erosion profile may change with implementation of the magnetic fields.

In order to assess the model, plasma potential and ion current density were compared with experimental data. The simulation results showed good agreement with the measurements, except near the centerline of the cathode. Changing potential boundary condition at the cathode inlet showed slightly better agreement in plasma potential in the cathode plume, implying that the cathode boundary condition plays an important role in the cathode plume. The erosion profile on the keeper is also sensitive to the cathode exit boundary condition.

Acknowledgments

The authors would like acknowledge support for this work from NASA Office of the Chief Technologist's Space Technology Research Fellowship (NSTRF), Grant #NNX11AN77H.

References

[1]Mikellides, I., Katz, I., Hofer, R., Goebel, D., "Magnetic shielding of the channel walls in a Hall plasma accelerator," *Physics of Plasmas*, 18, (2011): 033501.

[2]Hofer, R., Goebel, D., Mikellides, I., and Katz, I., "Design of a Laboratory Hall Thruster with Magnetically Shielded Channel Walls, Phase II: Experiments," Presented at 48th AIAA/ASME/SAE/ASEE Joint Propulsion Conference, AIAA-2012-3788, Atlanta, GA, July 2012.

[3]Hofer, R. R., Jorns, B. A., Polk, J. E., Mikellides, I. G., and Snyder, J. S, "Wear test of a magnetically shielded Hall thruster at 3000 seconds specific impulse," Presented at 33rd International Electric Propulsion Conference, Washington, DC., 2013.

[4]Goebel, D. M., Jorns, B. A., Hofer, R. R., Mikellides, I. G., and Katz, I., "Pole-piece Interactions with the Plasma in a Magnetically Shielded Hall Thruster," Presented at 50th AIAA/ASME/SAE/ASEE Joint Propulsion Conference, AIAA-2014-3899, Cleveland, OH, 28-30 July, 2014

[5]Goebel, D. and Katz. I., *Fundamentals of Electric Propulsion Ion and Hall Thrusters*, Vol.1, Hoboken, NJ: Wiley, 2008. Print.

[6]Goebel, D., Jameston, K., and Hofer, R., "Hall Thruster Cathode Flow Impact on Coupling Voltage and Cathode Life," *Journal of Propulsion and Power*, Vol. 28, No. 2 (2012): 355-363.

[7]Cai, C., "Theoretical and numerical studies of plume flows in vacuum chambers," Ph.D. Dissertation, Department of Aerospace Engineering, University of Michigan, Ann Arbor, MI, 2005.

[8]Bird, G. A., "Monte-Carlo simulation in an engineering context," *Progress in Astronautics and Aeronautics*, *74* (1981): 239-255.

[9]Miller, J. S., Pullins, S. H., Levandier, D. J., Chiu, Y. H., and Dressler, R. A., "Xenon charge exchange cross sections for electrostatic thruster models," *Journal of Applied Physics*, Vol. 91, No. 3 (2002): 984-991.

[10]Boyd, I. D., and Dressler, R. A., "Far field modeling of the plasma plume of a Hall thruster," *Journal of Applied Physics*, Vol. *92,* No. 4 (2002): 1764-1774.

[11]Boyd, I. D., and Yim, J. T., "Modeling of the near field plume of a Hall thruster," *Journal of Applied Physics*, Vol. 95 No. 9 (2004): 4575-4584.

[12]Yamamura, Y., and Tawara, H., "Energy Dependence of Ion-Induced Sputtering Yields from Monatomic Solids at Normal Incidence," *Atomic Data and Nuclear Data Tables,* Vol. 62, No. 2 (1996): 149-253.

[13]Pencil, E. J., Randolph, T., and Manzella, D. H., "End-of-Life Stationary Plasma Thruster Far-Field Plume Characterization," AIAA Paper No. 96-2709, 1996.

[14]Eckstein, W., Garcia-Rosales, C., and Roth, J., "Threshold Energy for Sputtering and Its Dependence on Angle of Incidence," *Nuclear Instruments and Methods in Physics Research B,* Vol. 83, (1993): 95-109.

[15]Gruber, J. R., "Low-Energy Sputter Erosion of Various Materials in a T5 Ion Thruster," Presented at 27th International Electric Propulsion Conference, IEPC-01-307, Fairview Park, OH, 2001.

[16]Doerner, R. P., Whyte, D. G., and Goebel, D. M., "Sputtering yield measurements during low energy xenon plasma bombardment," *Journal of Applied Physics,* Vol. 93, No. 9 (2003): 5816-5823.

[17]Kenmotsu, T., Wada, M., Hyakutake, T., Muramoto, T., and Nishida, M., "Enhanced sputtering yields of carbon due to accumulation of low-energy Xe ions." *Nuclear Instruments and Methods in Physics Research Section B: Beam Interactions with Materials and Atoms,* Vol. 267, No. 8 (2009): 1717-1720.

[18]Rosenberg, D., and Wehner, G. K., "Sputtering Yields for Low Energy He+-, Kr+-, and Xe+-Ion Bombardment," *Journal of Applied Physics,* Vol. 33, No. 5 (1962): 1842-1845.

[19]Williams, J. D, Gardner, M. M., Johnson, M. and Wilbur, P. J., "Xenon sputter yield measurements for ion thruster materials," National Aeronautics and Space Administration, NASA/CR-2003-212306, Glenn Research Center, Cleveland, OH, 2003.

[20]Williams, J. D., Johnson, M. L., and Williams, D. D., "Differential Sputtering Behavior of Pyrolytic Graphite and Carbon-Carbon Composite Under Xenon Bombardment," 40th AIAA/ASME/SAE/ASEE Joint Propulsion Conference, AIAA-2004-3788, Fort Lauderdale, FL, 2004.

[21]Kolasinski, R. D., Polk, J. E., Goebel, D., and Johnson, L. K., "Carbon sputtering yield measurements at grazing incidence," *Applied Surface Science,* Vol. 254, No. 8 (2008): 2506-2515.

[22]Huismann, T. D., "Improving hall thruster plume simulation through refined characterization of near-field plasma properties," Ph.D. Dissertation, Department of Aerospace Engineering, University of Michigan, Ann Arbor, MI, 2011.

[23]Choi, M., and Boyd, I. D., "Numerical Simulation of the Cathode Plume of a Hall Thruster," 50th AIAA/ASME/SAE/ASEE Joint Propulsion Conference, AIAA-2014-3427, Cleveland, OH, 2014.

[24]Mikellides, I. G., Katz, I., Goebel, D. M., and Polk, J. E. (2005). Hollow cathode theory and experiment. II. A two-dimensional theoretical model of the emitter region. *Journal of Applied Physics*, *98*(11), 113303.

[25]Jameson, K. K., "Investigation of hollow cathode effects on total thruster efficiency in a 6 kW Hall thruster," Ph.D. Dissertation, Department of Aerospace Engineering, University of California Los Angeles, Los Angeles, CA, 2008.

[26]Reid, B. M., "The influence of neutral flow rate in the operation of Hall thrusters," Ph.D. Dissertation, Department of Aerospace Engineering, University of Michigan, Ann Arbor, MI, 2009.